journal of the mechanical behavior of biomedical materials 128 (2022) 105129

Contents lists available at ScienceDirect

Journal of the Mechanical Behavior of Biomedical Materials

journal homepage: www.elsevier.com/locate/jmbbm

Changes in subchondral bone structure and mechanical properties do not substantially affect cartilage mechanical responses – A finite element study

Heta Orava [a,b,*], Lingwei Huang [a], Simo P. Ojanen [a,c], Janne T.A. Mäkelä [a], Mikko A.J. Finnilä [c], Simo Saarakkala [c], Walter Herzog [d], Rami K. Korhonen [a], Juha Töyräs [a,e,f], Petri Tanska [a]

[a] Department of Applied Physics, University of Eastern Finland, Kuopio, Finland
[b] Diagnostic Imaging Center, Kuopio University Hospital, Kuopio, Finland
[c] Research Unit of Medical Imaging, Physics and Technology, Faculty of Medicine, University of Oulu, Oulu, Finland
[d] Mechanical & Manufacturing Engineering, Schulich School of Engineering, University of Calgary, Calgary, Canada
[e] Science Service Center, Kuopio University Hospital, Kuopio, Finland
[f] School of Information Technology and Electrical Engineering, The University of Queensland, Brisbane, Australia

ARTICLE INFO

Keywords:
Articular cartilage
Fibril-reinforced poroelastic
Finite element analysis
Mechanical behavior
Subchondral bone

ABSTRACT

Subchondral bone structure has been observed to change in osteoarthritis (OA). However, it remains unclear how the early-stage OA changes affect the mechanics (stresses and strains) of the osteochondral unit. In this study, we aim to characterize the effect of subchondral bone structure and mechanical properties on the osteochondral unit mechanics. A 3-D finite element model of the osteochondral unit was constructed based on a rabbit femoral condyle μCT data and subjected to creep loading in indentation. Trabecular bone volume fraction, subchondral bone plate thickness, and equilibrium modulus were varied (including experimentally observed changes in early OA) to characterize the effect of these parameters on the osteochondral unit mechanics. At the end of the creep phase, the maximum principal strain at the bone surface of the cartilage-bone interface was decreased by 50% when the trabecular bone volume fraction was reduced from 48% to 28%. The maximum principal stress at the same location was decreased by 36% when plate thickness was reduced by 100 μm (−31%). In cartilage, small changes in the mechanics were seen near the cartilage-bone interface with a considerably thinner (−31%) plate. The changes in trabecular bone volume fraction, subchondral bone thickness and plate equilibrium modulus did not substantially affect the cartilage mechanics. Our results suggest that experimentally observed changes that occur in the subchondral bone structure in early OA have a minimal effect on cartilage mechanics under creep indentation loading; clear changes in the cartilage mechanics were seen only with an unrealistically soft subchondral bone plate.

1. Introduction

Mechanical factors play an important role in the onset and progression of osteoarthritis (OA) (Buckwalter and Martin, 2006; Burr and Schaffler, 1997). However, the mechanical interaction between cartilage and subchondral bone in the early stages of OA is still unclear (Goldring, 2012). For instance, Radin and Rose suggested that an increase in subchondral bone stiffness increases the stresses in cartilage and causes cartilage lesions (Radin and Rose, 1986). In some phenotypes of OA, it has been suggested that the earliest tissue alterations in OA occur in bone rather than cartilage (Mobasheri et al., 2017; Quasnichka et al., 2006; Zamli et al., 2014). However, it has not been directly shown how structural changes in bone affect cartilage mechanics, and how changes in cartilage mechanics might contribute to the progression of cartilage degeneration in OA. Therefore, research on how structural changes in bone may affect the mechanical interactions of the osteochondral unit appears warranted.

Post-traumatic knee OA has been induced with anterior cruciate ligament transection (ACLT) in many pre-clinical models. It causes instability of the joint (Laverty et al., 2010) and changes joint loading (Li et al., 2006) which is associated with adaptations in subchondral bone structure and morphology (Stewart and Kawcak, 2018). In the rat ACLT model, changes in the subchondral bone structure have been reported as soon as 2 weeks post-surgery (Hayami et al., 2006). Furthermore, in

* Corresponding author. Department of Applied Physics, University of Eastern Finland, POB 1627, FI-70211, Kuopio, Finland.
E-mail addresses: heta.orava@uef.fi (H. Orava), petri.tanska@uef.fi (P. Tanska).

https://doi.org/10.1016/j.jmbbm.2022.105129
Received 8 September 2021; Received in revised form 19 December 2021; Accepted 10 February 2022
Available online 13 February 2022

canine ACLT models, thinning of the subchondral bone plate and a decrease in the trabecular bone volume fraction have been reported at 10 and 20 weeks post-surgery (Intema et al., 2010; Sniekers et al., 2008). These structural changes in bone have been suggested to occur either simultaneously or even precede articular cartilage lesions (Lahm et al., 2006). In studies involving ACLT in rabbits, subchondral bone plate thinning and a decrease in trabecular bone volume have been reported at 4 and 8 weeks post-intervention (Batiste et al., 2004; Florea et al., 2015; Huang et al., 2021; Wang et al., 2007). Florea et al. (2015) reported that changes in lateral femoral cartilage precede the changes in bone, whereas, on the medial side, changes occurred simultaneously. Finally, bone changes have been observed to potentially precede cartilage degeneration in spontaneous guinea pig OA models (Chen et al., 2018; Quasnichka et al., 2006; Zamli et al., 2014). Taking together, it is still unclear whether the earliest post-traumatic OA changes occur first in cartilage or bone.

Experimental characterization of bone and cartilage mechanical behavior *in situ* is extremely challenging, if not impossible. The mechanical properties of bone and cartilage have been investigated *in vivo* simultaneously by using double upper and lower strain transducers in mechanical testing (Ding et al., 1998; Røhl et al., 1997) and by recording global deformations during mechanical testing with a high-speed camera (Malekipour et al., 2013, 2020; Shaktivesh et al., 2019). In turn, computational approaches, such as finite element (FE) modeling, allow the determination of the stresses and strains inside tissues. In most FE models, the focus has been on modeling either subchondral bone or articular cartilage rather than the whole osteochondral unit. Additionally, subchondral bone has often been considered rigid, as it has been suggested to cause only minor changes in contact pressures (Donahue et al., 2002; Shirazi and Shirazi-Adl, 2009). More recently, it has been suggested that the deformable subchondral bone may substantially affect cartilage mechanical responses, and thus consideration of this property might be important (Venäläinen et al., 2014, 2016b). Even in models of deformable bone, bones have been considered as a bulk structure and the trabecular bone architecture has often been neglected (Dar and Aspden, 2003; Shirazi and Shirazi-Adl, 2009; Stender et al., 2016, 2017). This representation may be an oversimplification, especially in view of recent findings suggesting that the porous structure of trabecular bone may contribute to site-specific cartilage stress and strain distributions (Venäläinen et al., 2014). Moreover, subchondral bone has typically been modeled as a linear elastic material, even though some structural characteristics may have been incorporated into the model geometry (Malekipour et al., 2016, 2017; Shirazi and Shirazi-Adl, 2009). Even though the elastic material assumption has been considered to be suitable for impact loading (Malekipour et al., 2016), it has been reported that trabecular bone may have time-dependent components (Fell et al., 2019; Manda et al., 2017; Ojanen et al., 2017; Xie et al., 2017) that might affect long-term mechanical responses near the cartilage-bone interface. Accounting for the structure of the entire osteochondral unit, combined with realistic material models for bone and cartilage, may help in understanding the mechanical interactions between cartilage and subchondral bone. In turn, this can provide novel insights into the mechanisms of onset and progression of OA.

Previously, Dar and Aspden (2003) modeled an idealized joint with isotropic, homogenous and linear elastic bone and cartilage material properties, and observed that neither bone thickness nor material properties affected the stresses in cartilage under impact loading conditions (Dar and Aspden, 2003). Further, previous knee joint models suggested that bone softening and reduction in the volume fraction of the trabecular bone structure reduce stresses in the knee joint cartilage in a site-specific manner (Venäläinen et al., 2014, 2016b).

In this study, we assume supported by the experimental observations that the structural changes in bone may precede those in cartilage in very early OA. With this assumption, we aim to characterize the effect of the subchondral bone structure and material properties on the mechanical responses of trabecular bone, subchondral bone plate, and articular cartilage. We account for the structural and material complexities in cartilage and bone to characterize the effect of subchondral bone structure and material properties on the mechanical behavior of the osteochondral unit, using advanced material models for bone and cartilage. Specifically, we investigate whether a reduction in trabecular bone volume fraction or subchondral bone plate thickness affects the articular cartilage mechanical behavior and reduces the stresses within cartilage. These objectives are investigated simulating a time-dependent loading condition (creep in an indentation geometry) applied to a rabbit osteochondral unit with a realistic subchondral bone structure that is obtained through μCT imaging.

2. Methods

2.1. Experiments and μCT imaging

An ACLT surgery was performed for six skeletally mature female New Zealand White rabbits (*Oryctolagus cuniculus*) ($n = 6$ knees). An age-matched non-operated control group of four rabbits ($n = 8$ knees) was used for comparison. The experiments and μCT imaging were conducted for a separate study (Huang et al., 2021) and are described in detail in Supplementary Material (Section A).

2.2. Finite element modeling

2.2.1. Geometry and FE model of the osteochondral junction

A lateral femoral condyle of a control knee joint was chosen as the reference geometry. A volume of interest (2 mm × 2 mm × height of the sample) of the central load-bearing area was chosen and μCT data of the lateral femoral condyle was segmented manually. The tetrahedral volumetric meshes for trabecular bone and subchondral bone plate were created using MATLAB (R2018b, The MathWorks Inc., Natick, MA, USA) and *iso2mesh* toolbox (v1.9, Fang and Boas, 2009). Then, variations on the subchondral bone plate and trabecular bone were conducted as described in section "Varying bone properties". The bone structures were imported into Abaqus/CAE (v2018, Dassault Systémes, USA) where cartilage was added to the FE model. A cartilage thickness of 330 μm was based on optical coherence tomography measurements. The total height of the reference model was 2.7 mm. Details on the geometry and meshing protocol are provided in Supplementary Material (Section B).

2.2.2. Material models and properties

Subchondral bone plate and trabecular bone were modeled as a hyper-viscoelastic material. The nonlinear elastic behavior was modeled using a Neo-Hookean strain energy potential and the viscoelastic behavior was modeled using a two-term Prony series. Subchondral bone plate and trabecular bone were assumed to have the same material properties. The bone material parameters were obtained from a previous nanoindentation study (Ojanen et al., 2017) and are presented in Table 1. The viscoelastic constitutive description was chosen 1) as we did not know how subchondral bone would behave under creep indentation loading and 2) to implement material level mechanical properties from nanoindentation measurements that are independent of tissue structure.

Cartilage was modeled as a fibril-reinforced poroelastic (FRPE) material consisting of a fluid and a porous solid matrix (Wilson et al., 2004), implemented in Abaqus using a user material (UMAT) script. This material model has been well-validated in the past (Julkunen et al., 2013; Korhonen et al., 2003; Li et al., 1999). The porous solid matrix further consists of a non-fibrillar part, representing proteoglycans, and a fibrillar part, representing the collagen fibril network. The fibrillar part consisted of four primary fibrils describing the arcade-like collagen network architecture, and 13 randomly oriented secondary fibrils (Tanska et al., 2020; Wilson et al., 2004). The collagen and water content and collagen structure were assumed depth-dependent, and the

Table 1
The geometry properties of the reference model and values of reference material parameters for bone and cartilage.

Reference model geometry properties					
Trabecular bone volume fraction (%)		Subchondral bone plate thickness (μm)		Cartilage thickness (μm)	
48		325		330	
Reference model material parameters					
Bone material parameters					
E_{eq} (MPa)	g_1	g_2	τ_1 (s)	τ_2 (s)	ν
2690	0.25	0.2	3.40	181	0.325
Cartilage material parameters					
E_f^0 (MPa)	E_f^e (MPa)	E_{nf} (MPa)	$k_0(10^{-15}m^4N^{-1}s^{-1})$	M	ν_{nf}
0.5500	19.6770	0.5726	0.6444	6.9472	0.42

E_{eq} equilibrium modulus, g_1 and g_2 normalized relaxation moduli, τ_1 and τ_2 short and long viscoelastic relaxation times, ν Poisson's ratio, E_f^0 initial fibril network modulus, E_f^e strain-dependent fibril network modulus, E_{nf} non-fibrillar matrix modulus, k_0 initial permeability, strain-dependent permeability coefficient, ν_{nf} non-fibrillar Poisson's ratio.

non-fibrillar matrix was assumed homogeneous. The material parameters for cartilage were obtained from the experimental stress-relaxation measurements by optimizing the mechanical force response to fit to the experimentally measured forces of the lateral femoral condyle control group. The material model, implementation and mechanical material parameters of cartilage are described in detail in the Supplementary Material (Section B). The cartilage material parameters were kept constant in all models (Table 1).

2.2.3. Loading and boundary conditions

The load was simulated as a force-controlled stress of 1 MPa, applied to the cartilage surface over 5 s and then held for an additional 300 s using a non-porous indenter. The cylindrical indenter ($d = 0.5$ mm) was modeled rigid, and its motion was controlled using a reference point on the surface of the indenter. This loading protocol can be replicated experimentally, and the magnitude of indentation loading and the creep application time were designed to match the global tissue strains observed in previous rabbit cartilage chondrocyte deformation studies with physiological loading magnitude and loading rate (Fick et al., 2015; Han et al., 2010; Tanska et al., 2020; Turunen et al., 2013). Force-controlled loading conditions were chosen, as the physiological loading condition within a knee joint resemble a force-controlled loading situation. Creep loading allows for studying both the instantaneous and equilibrium response of the tissues, and the instantaneous response of tissues reflects roughly 0.05 Hz dynamic or cyclic loading. Further, the indentation allowed studying the mechanical behavior outside of the indented area. The indenter diameter was small enough to minimize boundary effects (Spilker et al., 1992) and the cylindrical shape allowed the contact pressure to remain approximately the same throughout the creep loading.

The bottom nodes of the trabecular bone surface were fixed in the axial direction, and the side surface nodes of the bone parts were allowed to move only in the plane parallel to each side (Fig. S2). The top surface of the trabecular bone was fixed to the bottom surface of the subchondral bone plate, and the bottom surface of the cartilage was fixed to the top surface of the subchondral bone plate. A zero pore pressure (*i.e.*, free fluid flow) boundary condition was applied to the side and top surfaces of the cartilage, excluding the surface under the indenter. The contact between the indenter and cartilage was defined as a frictionless surface-to-surface contact. We also tested more uniform loading and different boundary conditions (see Supplementary Material, Section B).

2.2.4. Varying bone properties

The trabecular bone volume fraction and subchondral bone plate thickness of the segmented volume of interest of a lateral femoral condyle were varied with erosion and dilation operations on the trabecular bone and subchondral bone plate of the reference geometry. This was done to characterize the effect of bone structure on bone and cartilage stresses and strains. The parametric investigation included experimentally observed changes in trabecular bone volume fractions and subchondral bone thicknesses between the 8-week ACLT group and an age-matched control group (Huang et al., 2021) as well as values outside the experimentally observed range. Details on the experimentally observed changes are presented in Supplementary Material (Section B).

The trabecular bone volume fraction was varied using the iso2mesh toolbox (v1.9, Fang and Boas, 2009). From the experimentally measured 48% in the control animals, it was decreased to 38%, 28% and 20% using *thinbinvol* function and increased to 57% using *thickenbinvol* function. The functions either add or remove the boundary pixels of the volumetric binary image of the trabecular bone, and the trabecular bone volume fractions were calculated based on these newly obtained volumes. The thickness of the subchondral bone plate (325 μm) was parametrically varied, thickening it by +15% and thinning it by −15% and −31%. The thickening and thinning were performed by adding or removing pixels from everywhere at the top surface of the subchondral bone plate, *i.e.* the original structure with nonuniform thickness was increased or decreased by the same amount on the original surface architecture of the subchondral bone plate. For parametrical analysis of the material properties of the subchondral bone plate, the equilibrium modulus of the subchondral bone plate was parametrically altered to 150%, 50%, 25%, 5% and 0.2% of the original equilibrium modulus (2.69 GPa). Tetrahedral volumetric meshes were created similarly as done for the original reference geometry. Altogether, 13 different models were created: 7 of the 13 models had different geometry and 5 had different subchondral bone plate equilibrium modulus compared to the reference model (Table 2 and Fig. 1). Cartilage geometry and thickness were identical in all models (Huang et al., 2021, Table 1 and Fig. 1).

2.3. Analysis

Simulations were performed using Abaqus/Standard using soil consolidation analysis. We analyzed the maximum and minimum principal stresses and logarithmic strains as well as the maximum shear

Table 2
The parametrically modified geometry and material properties of the models. Only one bone model property was varied at a time. In addition to the reference model, 7 different geometries were created, and 5 models had varying subchondral bone plate equilibrium modulus. Altogether, 13 different models were created.

Model number	Modified model properties		
	Trabecular bone volume fraction (%)	Subchondral bone plate thickness (μm)	Subchondral bone plate equilibrium modulus (MPa)
1	48 (reference)	325 (reference)	2690 (reference)
2	**57**	325	2690
3	**38**	325	2690
4	**28**	325	2690
5	**20**	325	2690
6	48	**375**	2690
7	48	**275**	2690
8	48	**225**	2690
9	48	325	**4035**
10	48	325	**1345**
11	48	325	**673**
12	48	325	**135**
13	48	325	**5**

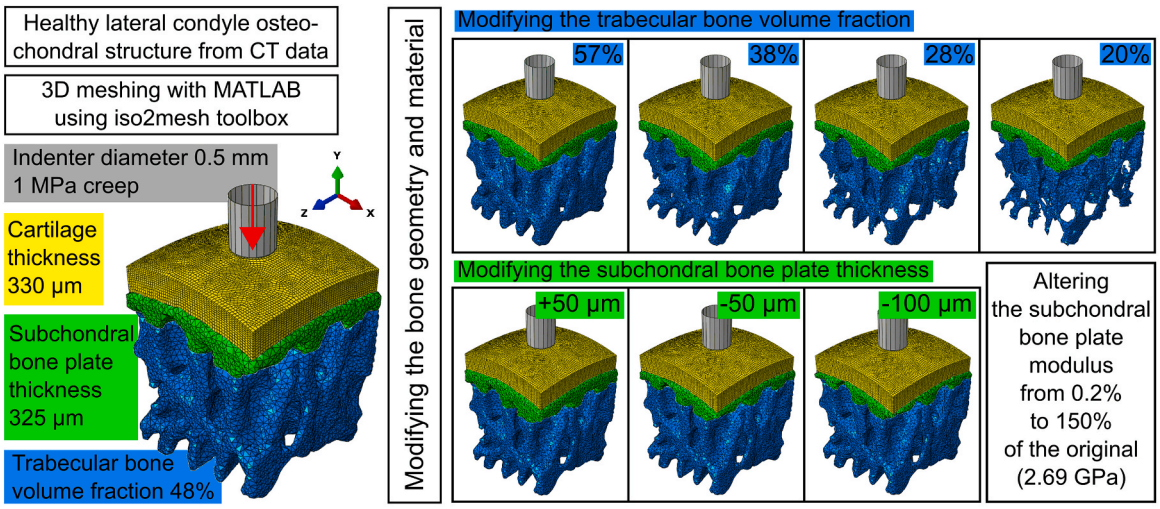

Fig. 1. Workflow of the study. The original bone geometry was obtained from segmented micro-computed tomography of a healthy lateral femoral condyle osteochondral structure and meshed using MATLAB (v2018b, iso2mesh toolbox). Cartilage was added on top of the subchondral bone plate. Mechanical indentation creep loading of 1 MPa was applied on the surface of the cartilage. The trabecular bone volume fraction and subchondral bone plate thickness were modified based on both experimentally observed changes and parametrical analysis. A parametrical analysis of the subchondral bone plate material properties was conducted by changing the bone plate equilibrium modulus to 150%, 50%, 25%, 5% and 0.2% of the original equilibrium modulus (2.69 GPa).

strain. Excessive minimum principal (compressive) and maximum shear strains are related to the failure of bone and the nonfibrillar matrix (proteoglycans) of cartilage as well as altered cell synthesis and/or death in cartilage (D'Lima et al., 2001; Gratz et al., 2008; Hosseini et al., 2014; Malekipour et al., 2017; Mononen et al., 2018; Nagaraja et al., 2005; Venäläinen et al., 2016a). The maximum principal (tensile) stresses and strains have been related to the failure of collagen fibrils in cartilage and tensile failure of the bone (Malekipour et al., 2017; Nagaraja et al., 2005; Sasazaki et al., 2006; Wilson et al., 2006).

The aforementioned parameters were qualitatively plotted in the mid-cross section of each model at the instantaneous (beginning) and "equilibrium" (end) phases of the creep. Additionally, they were quantitatively analyzed as a function of creep at the subchondral bone plate surface nodes, and at the cartilage deep zone nodes near the cartilage-bone interface (Supplementary Material, Section C). Moreover, compression of the articular cartilage, subchondral bone plate, and trabecular bone regions was evaluated using the approach provided in Supplementary Material (Section C).

3. Results

3.1. Varying trabecular bone volume fraction

In general, the maximum principal stresses and strains were increased in bone at the subchondral bone plate and trabecular bone below the indenter when the trabecular bone volume fraction was decreased, both at the beginning and at the end of the creep phase (Fig. 2). Similarly, compressive (minimum principal) stresses and strains in trabecular bone were larger when the trabecular bone volume fraction was decreased (Fig. 3A). The subchondral bone plate compressive strain was smaller when the trabecular bone volume fraction was decreased (Fig. 3C). In cartilage, the stress distributions did not vary between models (Figs. 2 and 3A). Specifically, at the end of creep, when the trabecular bone volume fraction was reduced to 20% from the original 48%, the averaged maximum principal stress at the subchondral bone plate surface at the cartilage-bone interface was increased by 45% (from 0.31 MPa to 0.45 MPa) (Fig. 2C). In addition, when the trabecular bone volume fraction was reduced to 28% from the original 48%, the maximum principal strain at the subchondral bone plate surface at the cartilage-bone interface was decreased by 50% (from 0.21×10^{-4} to 0.11×10^{-4}) (Fig. 2D).

The trabecular bone was compressed more when the trabecular bone volume fraction was decreased. At the end of creep, when the trabecular bone volume fraction was reduced to 20% from the original 48%, the trabecular bone compression was increased by 371% (from 0.10 to 0.47 µm) (Fig. 6B). Correspondingly, smaller compression was observed in the subchondral bone plate with a smaller trabecular bone volume fraction (Fig. 6A). Varying the trabecular bone volume fraction affected neither the stresses nor strains under investigation in the articular cartilage near the cartilage-bone interface at any time during the creep loading phase (Figs. 7 and 8).

3.2. Varying subchondral bone plate thickness

Overall, the maximum principal stresses and strains were increased in the subchondral bone plate and the trabecular bone below the indenter when the subchondral bone plate thickness was reduced. This result was obtained at the beginning and the end of the creep phase (Fig. 4). Especially, stresses and strains near the bone void at the interface between subchondral and trabecular bone increased when the subchondral bone plate was made thinner. Additionally, compressive stresses and strains were larger in the subchondral bone plate and the trabecular bone below the indenter when the subchondral bone plate thickness was reduced (Fig. 5). At the end of the creep phase, when the subchondral bone plate thickness was decreased from +50 µm to − 100 µm compared to the reference value observed, the maximum principal stress at the bone surface at the cartilage-bone interface was decreased by 36% (from 0.36 MPa to 0.26 MPa) (Fig. 4C). When the subchondral bone plate was 100 µm thinner than the reference, the maximum principal strain was increased by 150% at the end of the creep phase (from 0.21×10^{-4} to 0.52×10^{-4}) (Fig. 4D).

At the end of the creep phase, when the subchondral bone plate was 100 µm thinner than the reference thickness, the subchondral bone plate compression was increased by 8% (from 0.074 µm to 0.080 µm) (Fig. 6A). Similarly, when the subchondral bone plate was 100 µm thinner than the reference thickness, trabecular bone compression was increased by 17% (from 0.100 µm to 0.117 µm) (Fig. 6B). Stress distributions were similar in the articular cartilage for all bone plate thicknesses considered (Figs. 4 and 5), except for the location near the cartilage-bone interface, where a slight decrease in the maximum principal stresses (from 0.17 MPa to 0.16 MPa) and an increase in maximum principal strains (from 0.079 to 0.082) were observed when the bone

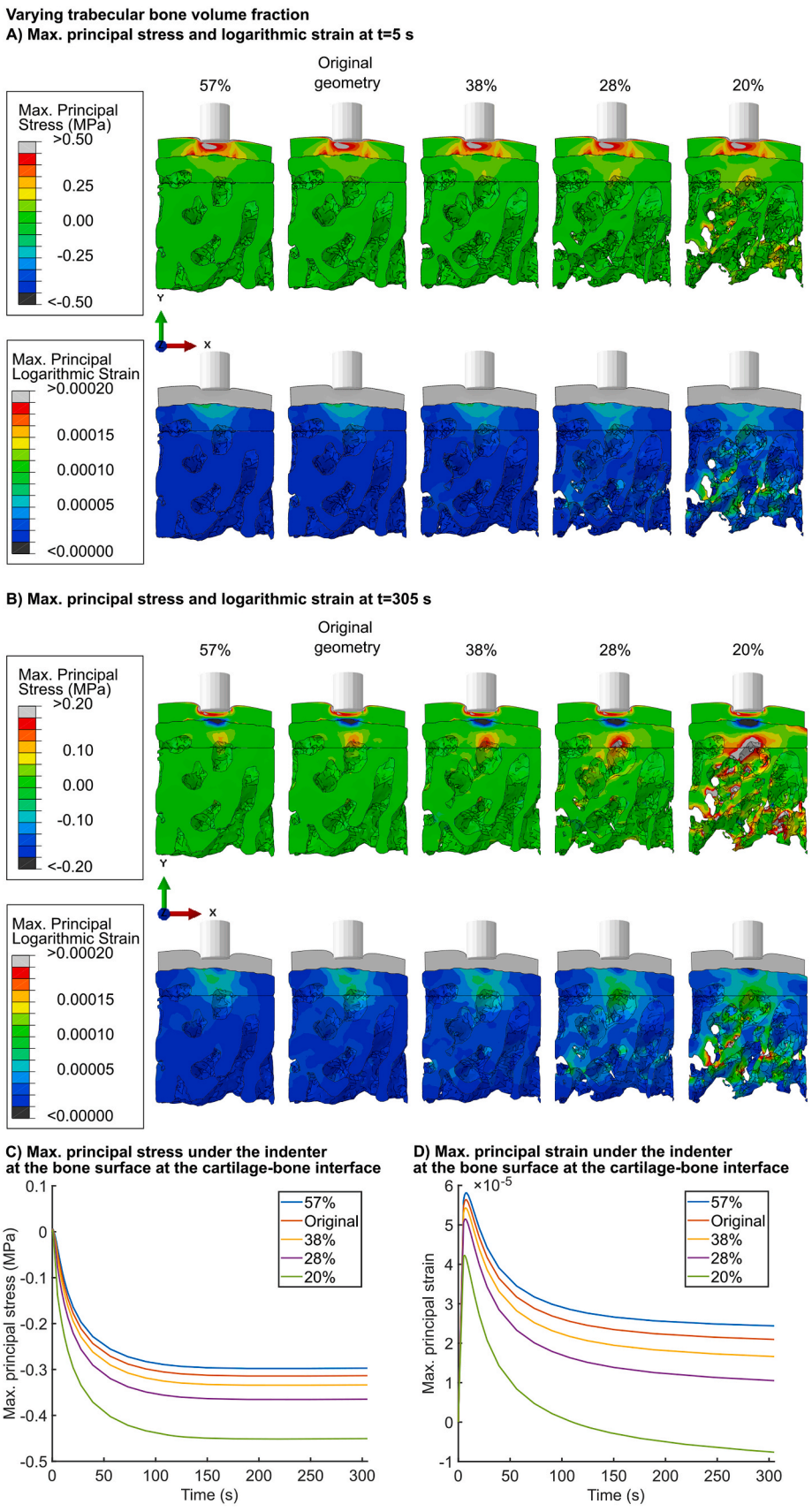

Fig. 2. A) Maximum principal stress (top row) and maximum principal strain (bottom row) in the mid-cross section of the models with varying trabecular bone volume fraction at t = 5 s (start of the creep i.e., during instantaneous response). B) Maximum principal stress (top row) and maximum principal strain (bottom row) in the mid-cross section of the models with varying trabecular bone volume fraction at t = 305 s. C) Maximum principal stress under the indenter, at the subchondral bone plate surface at the cartilage-bone interface with varying trabecular bone volume fraction. D) Maximum principal strain under the indenter, at the subchondral bone plate surface at the cartilage-bone interface with varying trabecular bone volume fraction. Note that in A) and B), the scale for max. principal stress is different.

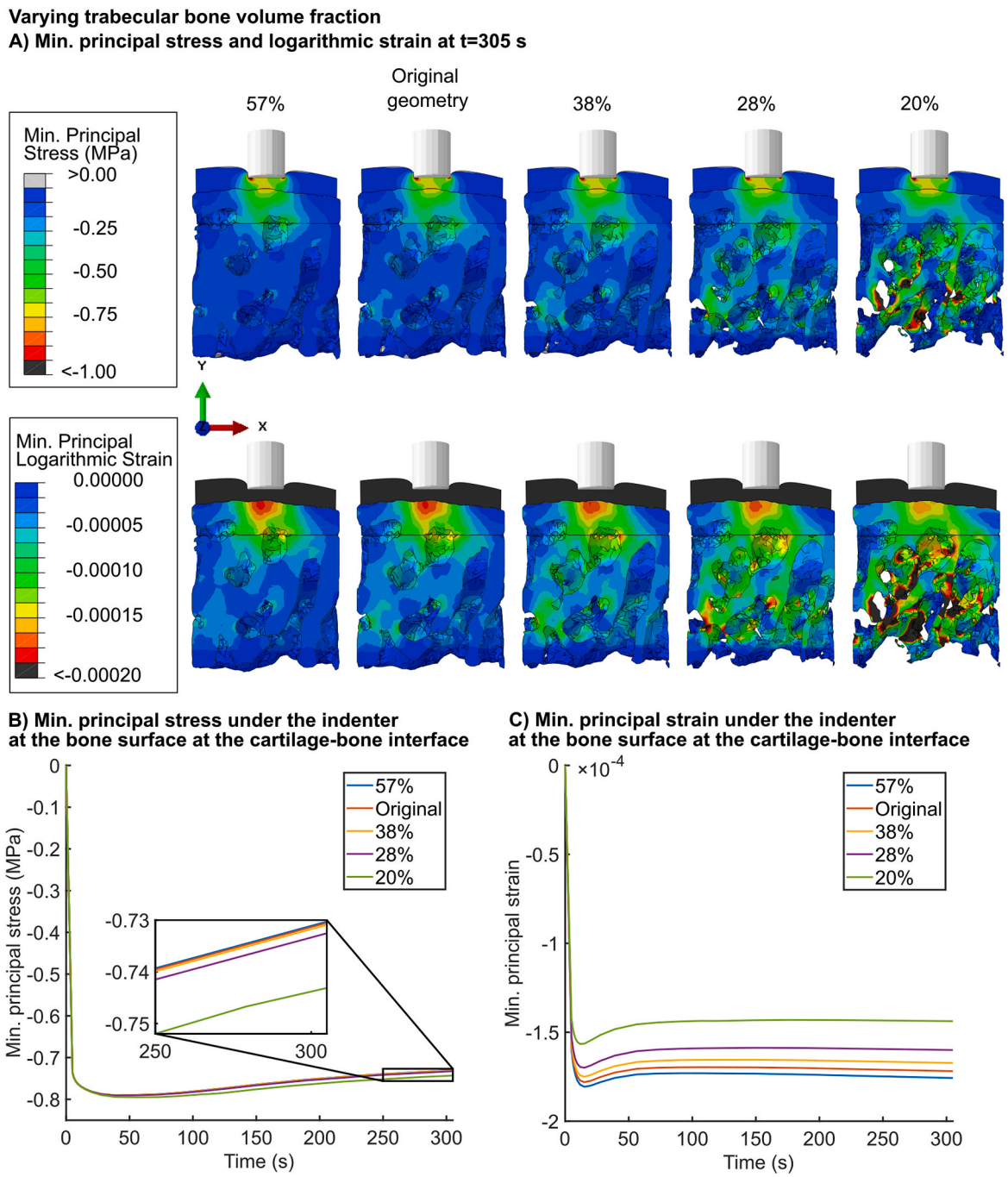

Fig. 3. A) Minimum principal stress (top row) and minimum principal strain (bottom row) in the mid-cross section of the models with varying trabecular bone volume fraction at t = 305 s. B) Minimum principal stress under the indenter, at the subchondral bone plate surface at the cartilage-bone interface with varying trabecular bone volume fraction. C) Minimum principal strain under the indenter, at the subchondral bone plate surface at the cartilage-bone interface with varying trabecular bone volume fraction.

plate thickness was decreased by 100 μm (Fig. 7). Additionally, the compressive strain and maximum shear strain in the cartilage near the cartilage-bone interface were slightly increased with the 100 μm thinner bone plate (from 0.56 to 0.57 and from 0.64 to 0.65, respectively) (Fig. 8).

3.3. Varying subchondral bone plate modulus

When the bone plate equilibrium modulus was reduced from the reference value to 25% and 5%, the subchondral bone plate deformation at the end of the creep was increased by 327% and 2100%, respectively (from 0.074 μm to 0.317 and 1.632 μm) (Fig. 6A). Correspondingly, when the bone plate equilibrium modulus was reduced from the reference value to 25% and 5%, the trabecular bone deformation was increased by 24% and 72%, respectively (from 0.100 μm to 0.124 and 0.172 μm) (Fig. 6B).

As observed with the varying subchondral bone plate thickness, when the equilibrium modulus was reduced from +50% to −50% of the reference value, the maximum principal stress below the indenter at the subchondral bone plate surface was reduced by 22% (from 0.35 MPa to 0.27 MPa) (Fig. 9A). Additionally, the maximum principal strain was increased by 181% (from 0.21 × 10^{-4} to 0.59 × 10^{-4}) when the

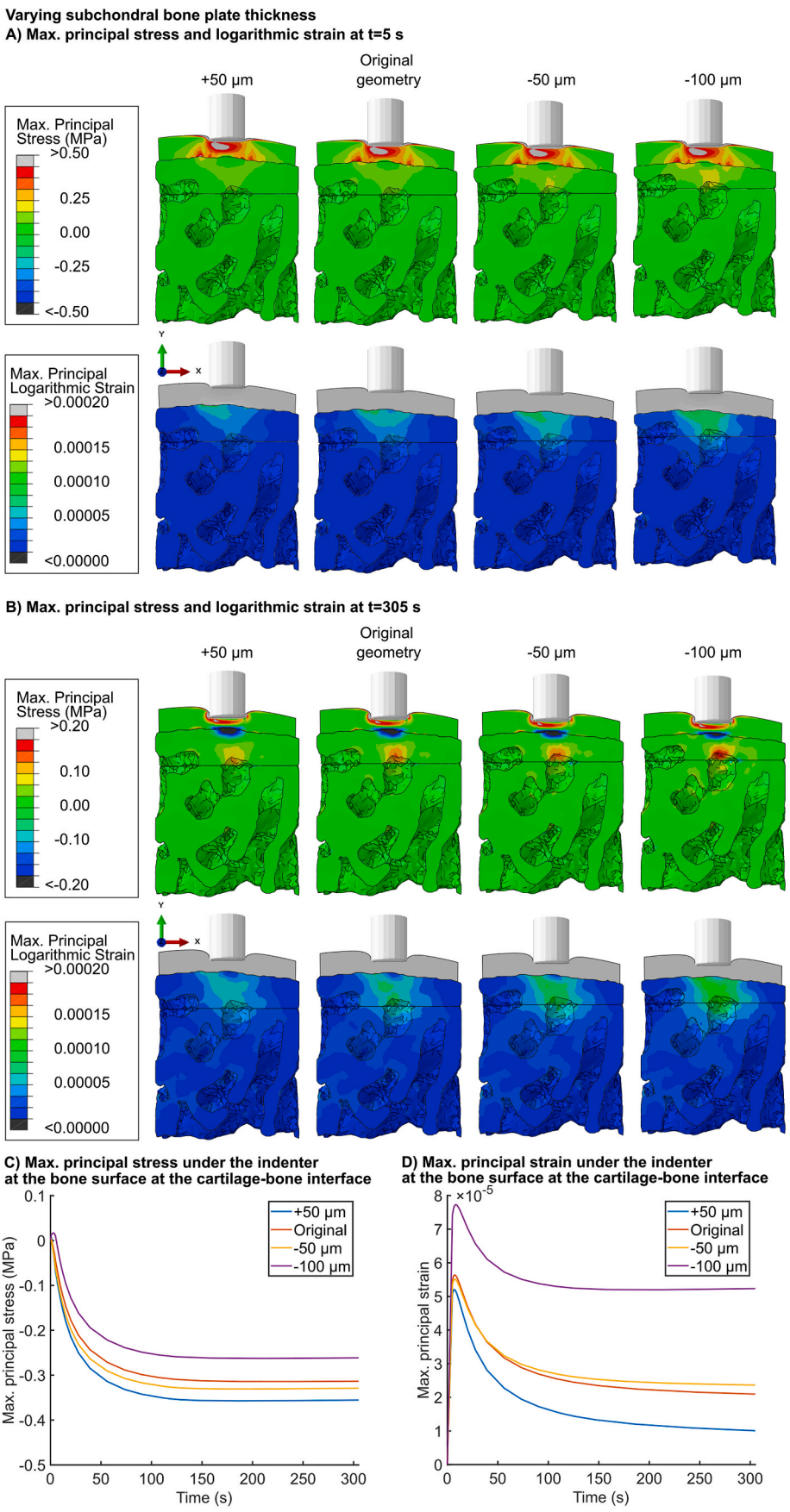

Fig. 4. A) Maximum principal stress (top row) and maximum principal strain (bottom row) in the mid-cross section of the models with varying subchondral bone plate thickness at t = 5 s (start of the creep i.e., during instantaneous response). B) Maximum principal stress (top row) and maximum principal strain (bottom row) in the mid-cross section of the models with varying subchondral bone plate thickness at t = 305 s. C) Maximum principal stress under the indenter, at the subchondral bone plate surface at the cartilage-bone interface with varying subchondral bone plate thickness. D) Maximum principal strain under the indenter, at the subchondral bone plate surface at the cartilage-bone interface with varying subchondral bone plate thickness. Note that in A) and B), the scale for max. principal stress is different.

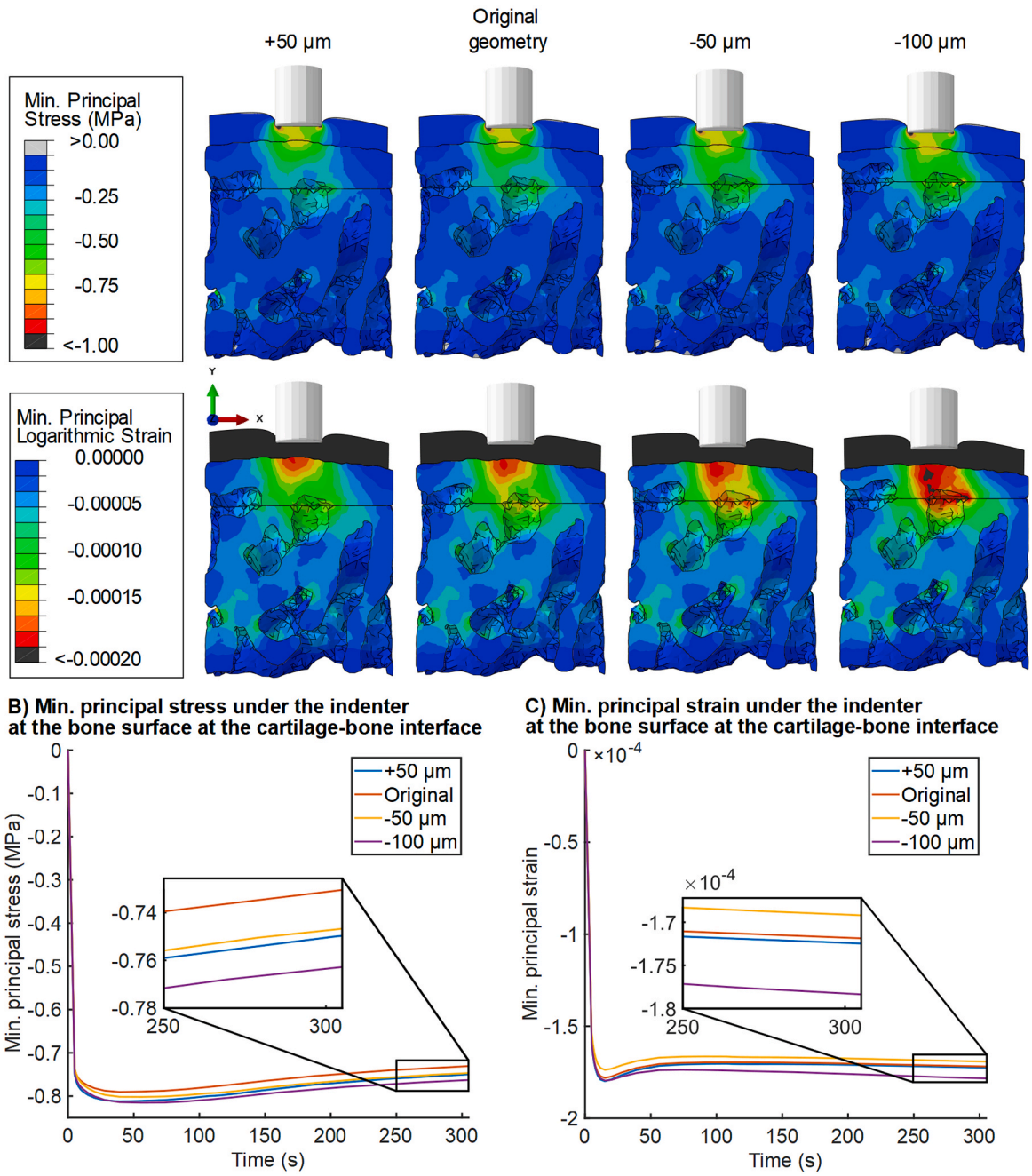

Fig. 5. A) Minimum principal stress (top row) and minimum principal strain (bottom row) in the mid-cross section of the models with varying subchondral bone plate thickness at t = 305 s. B) Minimum principal stress under the indenter, at the subchondral bone plate surface at the cartilage-bone interface with varying subchondral bone plate thickness. C) Minimum principal strain under the indenter, at the subchondral bone plate surface at the cartilage-bone interface with varying subchondral bone plate thickness.

equilibrium modulus was reduced by 50%, and by 600% (from 0.21 × 10^{-4} to 1.47 × 10^{-4}) when the equilibrium modulus was reduced to 25% (Fig. 9B). Interestingly, even when the equilibrium modulus of the subchondral plate was reduced to 5% of the original, there were no changes in cartilage stresses and strains. With the equilibrium modulus ranging from 5% to 150% of the reference value, the cartilage deformation at t = 5 s was 22% and 47% at the end of the creep phase. Noticeable changes were only observed when the subchondral bone plate was extremely soft, equilibrium modulus being 5 MPa (Fig. 7). At the end of the creep, the cartilage deformation reduced from 47% to 43% when the modulus was reduced to 0.2% of the reference value (Fig. 9C).

4. Discussion

A FE model consisting of a structurally realistic 3-D geometry of an osteochondral unit (2 mm × 2 mm × 2.7 mm) was created based on experimental µCT data of rabbit knee joints. Based on the experimental observations of changes in bone architecture in early OA, the trabecular bone volume fraction and the thickness of the subchondral bone plate were varied, and a sensitivity analysis with varying the equilibrium modulus of the subchondral bone plate was conducted. The model was subjected to creep loading in indentation to quantify whether the changes in bone properties affect the mechanical responses of bone and cartilage.

First, we observed that the trabecular bone volume fraction had a

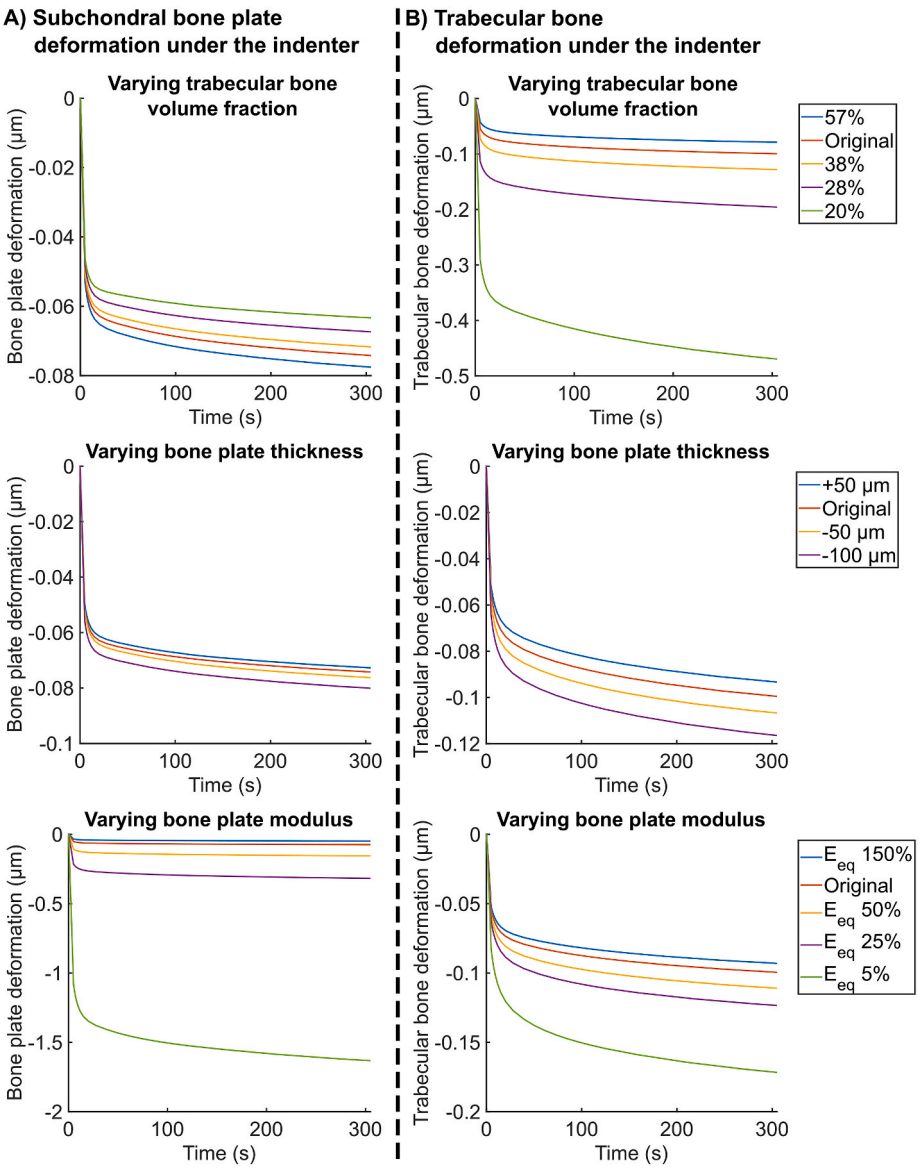

Fig. 6. A) The vertical deformation of subchondral bone plate under the indenter with varying trabecular bone volume fraction (top), subchondral bone plate thickness (middle) and subchondral bone plate equilibrium modulus (bottom). B) The vertical deformation of trabecular bone under the indenter with varying trabecular bone volume fraction (top), subchondral bone plate thickness (middle) and subchondral bone plate equilibrium modulus (bottom).

negligible effect on the stresses and strains experienced by the articular cartilage in indentation. This result is associated with the much greater stiffness of the bone than the cartilage so that even when the volume fraction of the bone is decreased, it does not affect the cartilage or the trabecular bone. Bone may be considered a very hard spring relative to cartilage, therefore, it does not matter how stiff the spring is, as long as it remains substantially stiffer than the cartilage. Venäläinen et al. (2014) investigated the effect of trabecular bone volume fraction in a two-dimensional human knee joint study and, when decreasing the bone volume fraction, reported a notable decrease in maximum principal stresses and strains in cartilage in the lateral tibial plateau, whereas, on the medial side, the decrease was substantially smaller, suggesting that the trabecular bone structure affects stresses in a site-specific manner (Venäläinen et al., 2014). In our model, the trabecular bone volume fraction did not affect the cartilage stresses, which might support the observation of site-specific behavior. However, in Venäläinen et al. the cartilage-bone interface was approximated as a smooth interface while in our study the interface was based on μCT segmentation. This might contribute to the differences between the studies. Sniekers et al. (2008) reported that changes in trabecular bone might not be directly related to changes in the subchondral bone plate and articular cartilage, suggesting that the subchondral bone plate might have a more pronounced effect on the onset of OA than the trabecular bone (Sniekers et al., 2008). This suggestion supports our observations that trabecular bone volume fraction does not affect the cartilage mechanical behavior.

In our second analysis, when the subchondral bone plate thickness was altered, only small changes in the maximum and minimum principal stresses and maximum and minimum principal and maximum shear strains in the cartilage near the cartilage-bone interface were observed. The thin subchondral bone plate caused a higher maximum principal strain in cartilage near the cartilage-bone interface than the thick plate because the bone plate deformed more when it was thinner. The maximum principal stress in cartilage near the cartilage-bone interface was slightly decreased with a thinning of the bone plate, which suggests that a reduction in subchondral bone thickness causes a decrease in cartilage stresses. Local changes in the subchondral bone plate surface topography result in locally varying stresses and strains in the cartilage near the cartilage-bone interface. In accordance with this, it has been

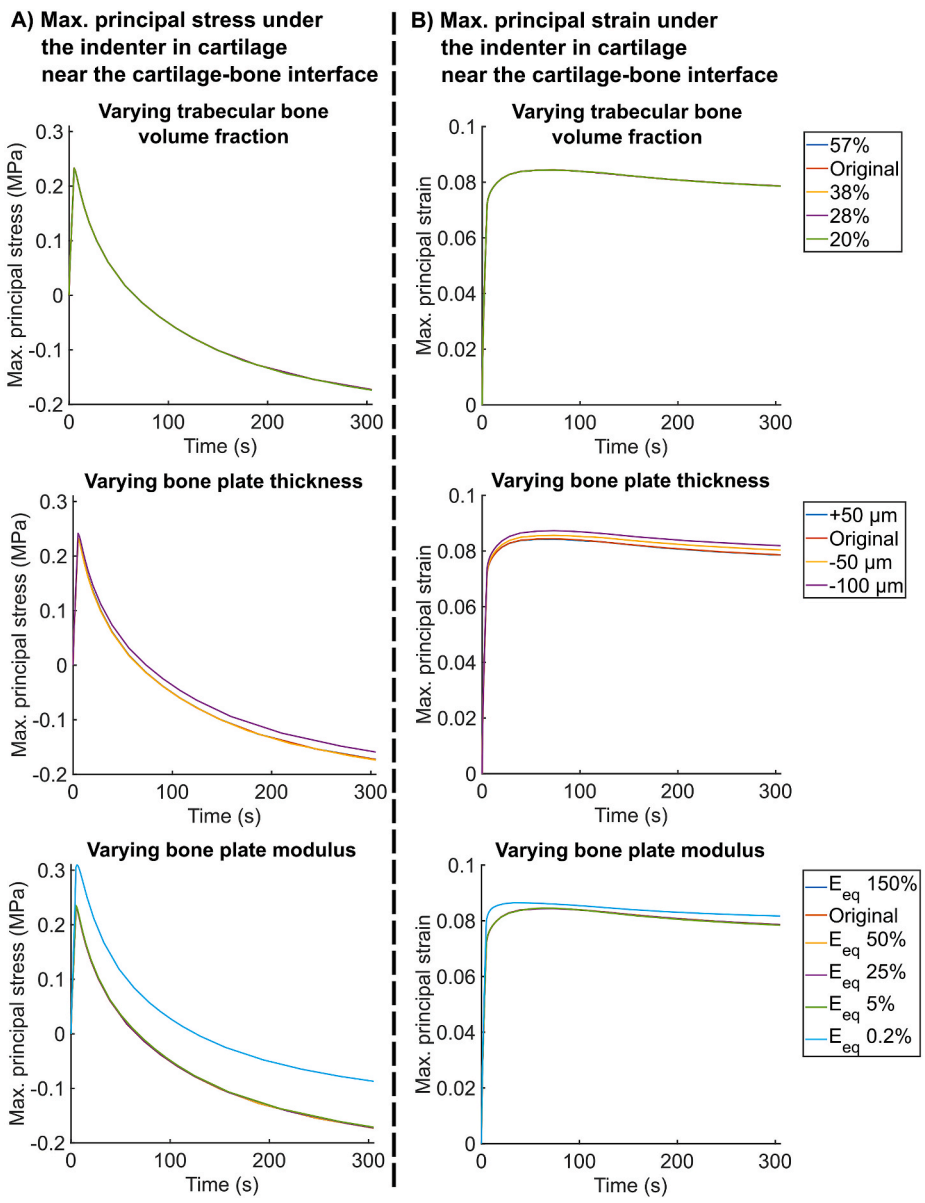

Fig. 7. A) Maximum principal stress under the indenter in cartilage near the cartilage-bone interface with varying trabecular bone volume fraction (top), subchondral bone plate thickness (middle) and subchondral bone plate equilibrium modulus (bottom). B) Maximum principal strain under the indenter in cartilage near the cartilage-bone interface with varying trabecular bone volume fraction (top), subchondral bone plate thickness (middle) and subchondral bone plate equilibrium modulus (bottom).

suggested that the inhomogeneity of the subchondral bone plate surface structure might lead to high tensile and shear stresses at the cartilage-bone interface (Li et al., 2013). Additionally, even though a large reduction in the subchondral plate thickness resulted only in small changes in cartilage stresses and strains, it is possible that subchondral bone plate may have a mechanical role in the onset and early progression of OA (Sniekers et al., 2008).

Finally, we analyzed the effect of subchondral bone plate equilibrium modulus on the mechanical responses of the osteochondral unit. When the subchondral bone plate equilibrium modulus was decreased, the maximum principal stresses in the subchondral bone were decreased and the strains were increased. At the same time, as one might expect, the subchondral bone plate deformed more, and the applied force caused higher maximum principal strains in the bone plate. Interestingly, the mechanical responses in the cartilage remained unaffected by the changes in the subchondral bone plate equilibrium modulus (from 5% to 150% of the reference value), and changes in cartilage deformation were not observed until the equilibrium modulus was decreased to 0.2% (5 MPa) of the reference value. Even if the subchondral bone plate equilibrium modulus was reduced to only 5% of the reference value, the equilibrium modulus was still greater than the cartilage equilibrium modulus that was ~1.2 MPa. Similarly, decreasing the trabecular bone volume fraction did not affect the stresses and strains in the cartilage to a measurable extent. Shirazi and Shirazi-Adl (2009) simulated the effects of osteochondral defects by locally decreasing the equilibrium modulus to 5 MPa in the calcified cartilage region and the subchondral bone plate near the trabecular bone surface. They observed that the maximum principal strain in the deep cartilage zone increased in the compromised area in a full knee joint model (Shirazi and Shirazi-Adl, 2009). This result is consistent with our analysis. We observed a decrease in the maximum principal stresses and an increase in the maximum principal strains in cartilage near the cartilage-bone interface when the subchondral bone plate equilibrium modulus was decreased to 5 MPa. Additionally, the total deformation of the cartilage was increased with the smallest equilibrium modulus used in our simulations. The unrealistically soft subchondral bone plate could be considered as representative of microdamage effects in subchondral bone, which can further affect the cartilage mechanical behavior, as observed with the 5 MPa plate equilibrium modulus. Malekipour et al. (2020) reported the stiffness of severely micro-damaged equine subchondral bone to be around

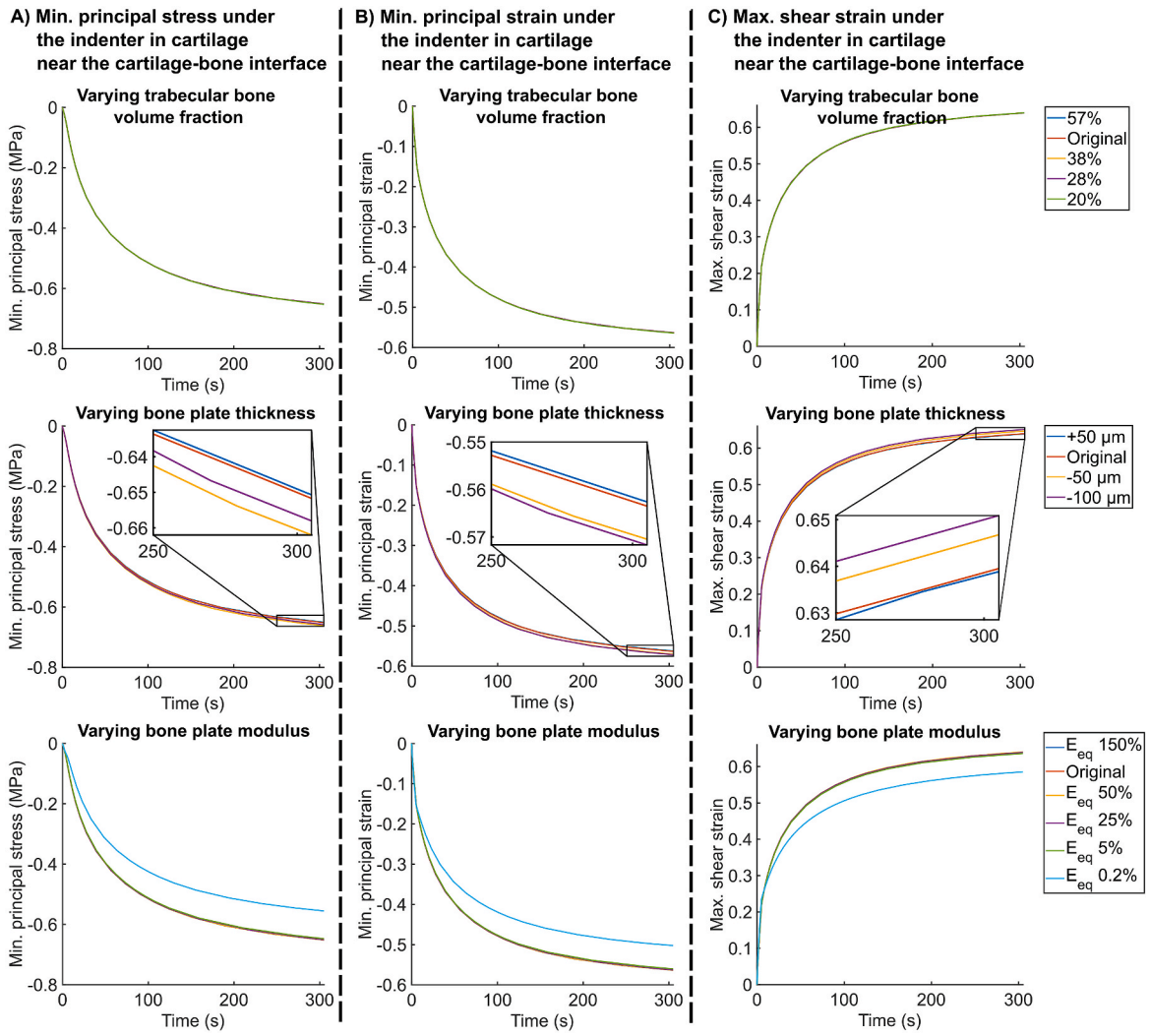

Fig. 8. A) Minimum principal stress under the indenter in cartilage near the cartilage-bone interface with varying trabecular bone volume fraction (top), subchondral bone plate thickness (middle), and subchondral bone plate equilibrium modulus (bottom). B) Minimum principal strain under the indenter in cartilage near the cartilage-bone interface with varying trabecular bone volume fraction (top), subchondral bone plate thickness (middle), and subchondral bone plate equilibrium modulus (bottom). C) Maximum shear strain under the indenter in cartilage near the cartilage-bone interface with varying trabecular bone volume fraction (top), subchondral bone plate thickness (middle), and subchondral bone plate equilibrium modulus (bottom). Graphs with different volume fractions (top) and equilibrium modulus values between 5% and 150% (bottom) are overlapping.

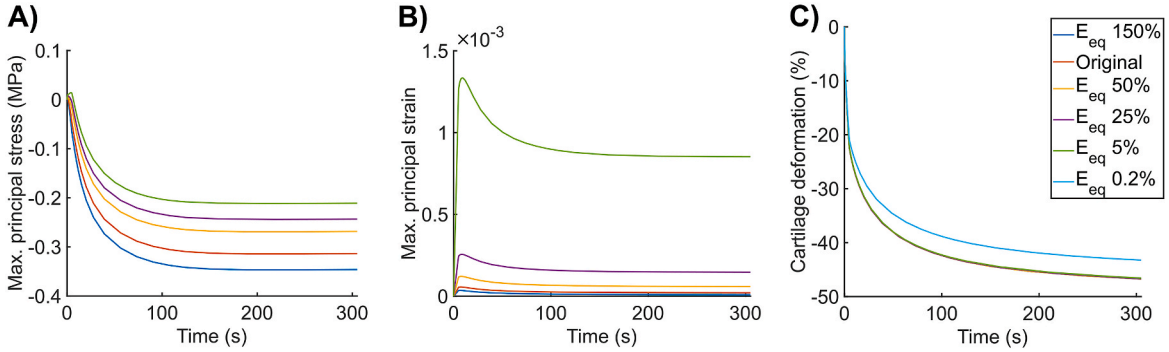

Fig. 9. A) Maximum principal stress under the indenter, at the subchondral bone plate surface at the cartilage-bone interface, B) Maximum principal strain under the indenter, at the subchondral bone plate surface at the cartilage-bone interface, C) Total cartilage deformation with varying subchondral bone plate modulus (graphs with equilibrium modulus values between 5% and 150% are overlapping).

20% of the nondamaged subchondral bone under single impact unconfined compression (Malekipour et al., 2020). Consequently, the smallest equilibrium modulus value used in this study may be too low an estimate, even for micro-damaged subchondral bone.

Previous results on the calcified cartilage stiffness have been variable: The macroscale calcified cartilage elastic modulus has been

reported to be an order of magnitude smaller than that of the subchondral bone (Hargrave-Thomas et al., 2015; Mente and Lewis, 1994). Simultaneously, the tissue-level calcified cartilage elastic modulus, obtained with nanoindentation, has been reported to be of the same order of magnitude as the subchondral bone plate elastic modulus (Ferguson et al., 2003; Gupta et al., 2005; Hargrave-Thomas et al., 2015; Pragnère et al., 2018). In previous computational studies, the Young's modulus of the calcified cartilage has been considered to be around 10% of the modulus of the subchondral bone (Sajjadinia et al., 2019; Shirazi and Shirazi-Adl, 2009; Stender et al., 2017). According to Stender et al. (2017), the exact properties of calcified tissues have little effect (presumably on the cartilage), which is supported by our analysis of the subchondral bone plate equilibrium modulus. Nevertheless, further studies including the transitional soft calcified layer are needed to elucidate the effect of tissue-level properties of this intermediate layer on the mechanical responses of the osteochondral unit. Further, the decrease in subchondral bone plate equilibrium modulus could also be interpreted as an investigation of how calcified cartilage softening may affect the mechanics of cartilage and trabecular bone. This analysis was made as we could not identify calcified cartilage using the present μCT protocol. Calcified cartilage is known to thicken in early OA through the advancement of the tidemark in the deep cartilage zone (Doube et al., 2007). Calcified cartilage also experiences a thinning and growth of new tidemarks via endochondral ossification (Doube et al., 2007; Lane and Bullough, 1980). These changes in the calcified cartilage with OA progression might play an important role in cartilage and bone interactions (Hayami et al., 2006). There might also be biochemical and -molecular crosstalk between bone and cartilage which might contribute to the progression of OA (Burr and Gallant, 2012; Findlay and Kuliwaba, 2016; Sharma et al., 2013). For instance, the elastic modulus of calcified cartilage was observed to decrease by 37% in rabbits six weeks after ACLT compared to a non-operated control group (Pragnère et al., 2018). This observation suggests that calcified cartilage mechanical properties change with OA progression and might affect the mechanical behavior of bone and non-calcified cartilage. Thus, we aim to include calcified cartilage in future osteochondral models of joint contact behavior. However, including the calcified cartilage requires high-resolution μCT (Mehadji et al., 2019; Rytky et al., 2021) or synchrotron CT imaging (Portier et al., 2020) methods of osteochondral junction identification.

Our study is based on the assumption that structural and mechanical changes in bone precede the corresponding changes in cartilage in early OA. Thus, we focused on characterizing the effects of bone structure on the osteochondral unit while maintaining the cartilage material properties and geometries for all models. This can be considered as a limitation of our study since the post-traumatic ACLT model may not truly simulate the subchondral bone-driven OA phenotype. For instance, Pragnère et al. (2018) observed that in rabbits, the decrease in the elastic modulus was greater in articular cartilage than in bone 6 weeks after ACLT compared to the control group. Based on these observations, they suggested that the changes in cartilage might occur prior to those in bone (Pragnère et al., 2018). However, the choice of keeping the cartilage geometry constant across models is also justified based on experiments, as the thickness of the cartilage in the lateral femoral condyles did not change between the healthy control and ACLT group rabbits (Huang et al., 2021).

Experimental data corresponding to the exact loading scenario used in our study was not available. Nevertheless, the cartilage material parameters were obtained from the stress-relaxation experiments conducted for the rabbits from which the reference geometry was obtained, and replicating the experimentally measured force responses computationally, combining optimization and FE modeling. Additionally, the bone properties were obtained from a previous nanoindentation study (Ojanen et al., 2017) using a similar approach to the one used here for cartilage. Even though the model size was moderate, the thickness of the bone portion is close to what has been considered large enough compared to the cartilage to not affect the results (Burgin and Aspden, 2007). Even if the bone thickness had a slight effect on the results, the comparison of the results and conclusions would not be affected as the thickness ratio between bone and cartilage thickness is similar in all models.

Maintaining the cartilage material properties same in all models was justified as the equilibrium and dynamic moduli of articular cartilage in the lateral femoral condyles did not vary between the healthy control and ACLT group rabbits (Kajabi et al., 2020), although OARSI grading scores were statistically greater in the ACLT group animals (Huang et al., 2021). This discrepancy between cartilage structure and cartilage properties may be explained by the fact that the collagen network integrity was only minimally changed in these rabbits while the proteoglycan loss (and partial recovery) was clearly observable by the greater OARSI grade in the ACLT compared to the control group animals. The proteoglycan content of the cartilage, reflected by the non-fibrillar matrix modulus, was considered homogeneous throughout the tissue, even though it has been shown to vary as a function of cartilage depth (Kiviranta et al., 1985; Räsänen et al., 2016). The non-fibrillar matrix modulus has been shown to be the main parameter defining the cartilage mechanical response at equilibrium (Halonen et al., 2013; Räsänen et al., 2016), which was not fully reached in the creep loading condition used in this study. In indentation testing, the collagen network also contributes to the mechanical response at equilibrium, and thus it may compensate for the tissue degradation caused by the loss of proteoglycans.

Different material properties for cartilage would naturally affect the mechanical behavior of cartilage. Other OA-like changes in cartilage material properties, such as greater permeability and smaller initial fibril network modulus, would mainly affect the instantaneous and early temporal creep responses, as cartilage would be expected to deform more during early compression due to the lack of fluid pressurization and tensile recruitment of collagen fibers, while the loss of proteoglycans, reflected by the non-fibrillar matrix modulus, mainly affects the mechanical response at equilibrium. However, even with altered cartilage properties, the current conclusion of a minimal effect of bone on cartilage stresses and strains would not be changed as the cartilage properties would be even softer in OA and the stiffness difference between cartilage and bone would be even greater than simulated here. Based on these considerations, it is reasonable to assume that the mechanical changes of the calcified cartilage and/or the superficial subchondral bone plate are more important than those in the cartilage as they might be the key factors for cartilage thinning through endochondral ossification and deep cartilage calcification.

In this study, the cartilage thickness was the same for all models. Cartilage deformation, being 22% at the beginning of the creep and 47% at the end of the creep, was in a similar range to what has been observed in physiological loading of knee joints: peak contact deformations up to 30% have been reported during flexion (Bingham et al., 2008), up to 23% during the gait cycle (Liu et al., 2010), and up to 39% after 30 min of standing (Halonen et al., 2014). As was observed with rabbits (Huang et al., 2021), cartilage thickness (330 μm) was similar to the subchondral bone plate thickness (225–375 μm). However, human cartilage is substantially thicker than human subchondral bone plate (Bhatla et al., 2018) and further studies are required to investigate if the observed cartilage mechanical behavior applies for the thicker human cartilage.

The instantaneous response at the beginning of the creep loading remained unaltered when the trabecular bone volume fraction and subchondral bone plate thickness were modified. As the mechanical response of dynamic or cyclic loading corresponds to the instantaneous response, similar conclusions would be obtained with cyclic or dynamic loading. Under uniform loading, the overall stresses and strains were decreased compared to indentation, and they were more uniformly distributed in the osteochondral unit. Altogether, the observed changes are expected, and they do not change the conclusions. As the cartilage mechanical responses remained unaltered when changing the bone boundary conditions, and in bone, the changes had a similar trend in all

models, the boundary conditions do not affect the conclusions.

In conclusion, we suggest that the structural alterations in trabecular bone and the subchondral bone plate that occur in the rabbit model of early OA affect the stresses and strains in bone, but do not affect, or only minimally so, the stresses and strains in the articular cartilage under creep indentation loading. Previously, it has been shown that the stiffness of subchondral bone does not affect the cartilage stresses under impact loading, with homogenous linear elastic material models in a simplified joint geometry (Dar and Aspden, 2003). Our results expand the previous conclusion by Dar et al. (2003) to apply to time-dependent loading response, with realistic osteochondral unit structure and advanced material models for bone and cartilage. Stresses and strains of cartilage were altered only when the plate was thinned considerably, or when it was assumed to be extremely soft. Yet, further investigations of these mechanisms e.g. in the whole knee joint model are required. Changes in the stress and strain environment at the cartilage-bone interface might suggest a new biomechanically driven mechanism for tissue remodeling, adaptation, and progression of OA in bone and cartilage. To obtain deeper insight into this topic, samples at different stages of OA should be carefully studied for structural alterations and associated mechanical changes in the same rabbit model as used here. The obtained modeling results could also be validated *in situ* using confocal microscopy (Price et al., 2010; Verbruggen et al., 2015). Furthermore, the approach used here should be implemented in a rabbit knee joint model utilizing a more realistic loading environment, corresponding to in vivo behavior of the osteochondral unit.

Author contributions

Heta Orava: Conceptualization, Methodology, Software, Validation, Formal analysis, Writing - Original Draft, Visualization, Funding acquisition.

Lingwei Huang: Investigation, Writing - Review & Editing.

Simo P. Ojanen: Investigation, Writing - Review & Editing.

Janne T. A. Mäkelä: Investigation, Resources, Writing - Review & Editing.

Mikko A. J. Finnilä: Conceptualization, Methodology, Investigation, Resources, Writing - Review & Editing.

Simo Saarakkala: Conceptualization, Methodology, Investigation, Resources, Writing - Review & Editing.

Walter Herzog: Conceptualization, Methodology, Investigation, Resources, Writing - Review & Editing.

Rami K. Korhonen: Conceptualization, Methodology, Investigation, Resources, Writing - Review & Editing, Supervision, Project administration, Funding acquisition.

Juha Töyräs: Conceptualization, Methodology, Resources, Writing - Review & Editing, Supervision, Project administration, Funding acquisition.

Petri Tanska: Conceptualization, Methodology, Validation, Formal analysis, Resources, Writing - Original Draft, Visualization, Project administration, Funding acquisition.

Role of the funding source

The research leading to these results has received funding from the Academy of Finland (#307932, #324529), Strategic funding of the University of Eastern Finland, Research Committee of the Kuopio University Hospital Catchment Area for the State Research Funding (#5041788), Finnish Cultural Foundation – Central Fund (#191044, #00180796), Kymenlaakso regional fund (#35201579) and North Savo regional fund (#65171624), Sigrid Juselius Foundation, Maire Lisko Foundation, Alfred Kordelin Foundation (#190317), Saastamoinen Foundation, Päivikki and Sakari Sohlberg Foundation and Emil Aaltonen Foundation. The funding sources had no role in the study design, collection, analysis and interpretation of data; in the writing of the manuscript; and in the decision to submit the manuscript for publication.

Declaration of competing interest

The authors declare that they have no known competing financial interests or personal relationships that could have appeared to influence the work reported in this paper.

Acknowledgments

CSC—IT Center for Science Ltd., Finland is acknowledged for providing computational resources and modeling software. Esko Järvinen, Jarmo Pirhonen and Sampo Sillanpää, employees of CSC, are acknowledged for providing help and support in cluster implementation of the model. The Canada Research Chair Programme, the Canadian Institutes for Health Research, and the Killam Foundation are acknowledged for funding the animal experiments described in this study.

Appendix A. Supplementary data

Supplementary data to this article can be found online at https://doi.org/10.1016/j.jmbbm.2022.105129.

References

Batiste, D.L., Kirkley, A., Laverty, S., Thain, L.M.F., Spouge, A.R., Holdsworth, D.W., 2004. Ex vivo characterization of articular cartilage and bone lesions in a rabbit ACL transection model of osteoarthritis using MRI and micro-CT. Osteoarthritis Cartilage 12, 986–996. https://doi.org/10.1016/j.joca.2004.08.010.

Bhatla, J.L., Kroker, A., Manske, S.L., Emery, C.A., Boyd, S.K., 2018. Differences in subchondral bone plate and cartilage thickness between women with anterior cruciate ligament reconstructions and uninjured controls. Osteoarthritis Cartilage 26, 929–939. https://doi.org/10.1016/j.joca.2018.04.006.

Bingham, J.T., Papannagari, R., Van de Velde, S.K., Gross, C., Gill, T.J., Felson, D.T., Rubash, H.E., Li, G., 2008. In vivo cartilage contact deformation in the healthy human tibiofemoral joint. Rheumatology 47, 1622–1627. https://doi.org/10.1093/RHEUMATOLOGY/KEN345.

Buckwalter, J.A., Martin, J.A., 2006. Osteoarthritis. Adv. Drug Deliv. Rev. 58, 150–167. https://doi.org/10.1007/978-3-319-59963-2_9.

Burgin, L.V., Aspden, R.M., 2007. Impact testing to determine the mechanical properties of articular cartilage in isolation and on bone. J. Mater. Sci. Mater. Med. 19, 703–711. https://doi.org/10.1007/S10856-007-3187-2.

Burr, D.B., Gallant, M.A., 2012. Bone remodelling in osteoarthritis. Nat. Rev. Rheumatol. 8, 665–673. https://doi.org/10.1038/nrrheum.2012.130.

Burr, D.B., Schaffler, M.B., 1997. The involvement of subchondral mineralized tissues in osteoarthrosis: quantitative microscopic evidence. Microsc. Res. Tech. 37, 343–357. https://doi.org/10.1002/(SICI)1097-0029(19970515)37:4<343:AID-JEMT9>3.0.CO;2-L.

Chen, Y., Hu, Y., Yu, Y.E., Zhang, X., Watts, T., Zhou, B., Wang, J., Wang, T., Zhao, W., Chiu, K.Y., Leung, F.K.L., Cao, X., Macaulay, W., Nishiyama, K.K., Shane, E., Lu, W. W., Guo, X.E., 2018. Subchondral trabecular rod loss and plate thickening in the development of osteoarthritis. J. Bone Miner. Res. 33, 316–327. https://doi.org/10.1002/jbmr.3313.

D'Lima, D.D., Hashimoto, S., Chen, P.C., Lotz, M.K., Colwell, C.W., 2001. Cartilage injury induces chondrocyte apoptosis. J. Bone Jt. Surg. 83-A, 19–21.

Dar, F.H., Aspden, R.M., 2003. A finite element model of an idealized diarthrodial joint to investigate the effects of variation in the mechanical properties of the tissues. Proc. Inst. Mech. Eng. Part H J. Eng. Med. 217, 341–348. https://doi.org/10.1243/095441103770802504.

Ding, M., Dalstra, M., Linde, F., Hvid, I., 1998. Mechanical properties of the normal human tibial cartilage-bone complex in relation to age. Clin. Biomech. 13, 351–358. https://doi.org/10.1016/S0268-0033(98)00067-9.

Donahue, T.L.H., Hull, M.L., Rashid, M.M., Jacobs, C.R., 2002. A finite element model of the human knee joint for the study of tibio-femoral contact. J. Biomech. Eng. 124, 273–280. https://doi.org/10.1115/1.1470171.

Doube, M., Firth, E.C., Boyde, A., 2007. Variations in articular calcified cartilage by site and exercise in the 18-month-old equine distal metacarpal condyle. Osteoarthritis Cartilage 15, 1283–1292. https://doi.org/10.1016/j.joca.2007.04.003.

Fang, Q., Boas, D.A., 2009. Tetrahedral mesh generation from volumetric binary and gray-scale images. In: IEEE International Symposium on Biomedical Imaging: from Nano to Macro, pp. 1142–1145. https://doi.org/10.1109/ISBI.2009.5193259.

Fell, N.L.A., Lawless, B.M., Cox, S.C., Cooke, M.E., Eisenstein, N.M., Shepherd, D.E.T., Espino, D.M., 2019. The role of subchondral bone, and its histomorphology, on the dynamic viscoelasticity of cartilage, bone and osteochondral cores. Osteoarthritis Cartilage 27, 535–543. https://doi.org/10.1016/j.joca.2018.12.006.

Ferguson, V.L., Bushby, A.J., Boyde, A., 2003. Nanonmechanical properties and mineral concentration in articular calcified cartilage and subchondral bone. J. Anat. 203, 191–202. https://doi.org/10.1046/j.1469-7580.2003.00193.x.

Fick, J.M., Ronkainen, A., Herzog, W., Korhonen, R.K., 2015. Site-dependent biomechanical responses of chondrocytes in the rabbit knee joint. J. Biomech. 48, 4010–4019. https://doi.org/10.1016/j.jbiomech.2015.09.049.

Findlay, D.M., Kuliwaba, J.S., 2016. Bone–cartilage crosstalk: a conversation for understanding osteoarthritis. Bone Res 4, 16028. https://doi.org/10.1038/boneres.2016.28.

Florea, C., Malo, M.K.H., Rautiainen, J., Mäkelä, J.T.A., Fick, J.M., Nieminen, M.T., Jurvelin, J.S., Davidescu, A., Korhonen, R.K., 2015. Alterations in subchondral bone plate, trabecular bone and articular cartilage properties of rabbit femoral condyles at 4 weeks after anterior cruciate ligament transection. Osteoarthritis Cartilage 23, 414–422. https://doi.org/10.1016/j.joca.2014.11.023.

Goldring, S.R., 2012. Alterations in periarticular bone and cross talk between subchondral bone and articular cartilage in osteoarthritis. Ther. Adv. Musculoskelet. Dis. 4, 249–258. https://doi.org/10.1177/1759720X12437353.

Gratz, K.R., Wong, B.L., Bae, W.C., Sah, R.L., 2008. The effects of focal articular defects on intra-tissue strains in the surrounding and opposing cartilage. Biorheology 45, 193–207. https://doi.org/10.3233/BIR-2008-0475.

Gupta, H.S., Schratter, S., Tesch, W., Roschger, P., Berzlanovich, A., Schoeberl, T., Klaushofer, K., Fratzl, P., 2005. Two different correlations between nanoindentation modulus and mineral content in the bone–cartilage interface. J. Struct. Biol. 149, 138–148. https://doi.org/10.1016/J.JSB.2004.10.010.

Halonen, K.S., Mononen, M.E., Jurvelin, J.S., Töyräs, J., Korhonen, R.K., 2013. Importance of depth-wise distribution of collagen and proteoglycans in articular cartilage-A 3D finite element study of stresses and strains in human knee joint. J. Biomech. 46, 1184–1192. https://doi.org/10.1016/j.jbiomech.2012.12.025.

Halonen, K.S., Mononen, M.E., Jurvelin, J.S., Töyräs, J., Salo, J., Korhonen, R.K., 2014. Deformation of articular cartilage during static loading of a knee joint - experimental and finite element analysis. J. Biomech. 47, 2467–2474. https://doi.org/10.1016/j.jbiomech.2014.04.013.

Han, S.-K., Seerattan, R., Herzog, W., 2010. Mechanical loading of in situ chondrocytes in lapine retropatellar cartilage after anterior cruciate ligament transection. J. R. Soc. Interface 7, 895–903. https://doi.org/10.1098/rsif.2009.0458.

Hargrave-Thomas, E., van Sloun, F., Dickinson, M., Broom, N., Thambyah, A., 2015. Multi-scalar mechanical testing of the calcified cartilage and subchondral bone comparing healthy vs early degenerative states. Osteoarthritis Cartilage 23, 1755–1762. https://doi.org/10.1016/j.joca.2015.05.012.

Hayami, T., Pickarski, M., Zhuo, Y., Wesolowski, G.A., Rodan, G.A., Duong, L.T., 2006. Characterization of articular cartilage and subchondral bone changes in the rat anterior cruciate ligament transection and meniscectomized models of osteoarthritis. Bone 38, 234–243. https://doi.org/10.1016/j.bone.2005.08.007.

Hosseini, S.M., Wilson, W., Ito, K., Van Donkelaar, C.C., 2014. A numerical model to study mechanically induced initiation and progression of damage in articular cartilage. Osteoarthritis Cartilage 22, 95–103. https://doi.org/10.1016/J.JOCA.2013.10.010.

Huang, L., Riihioja, I., Tanska, P., Ojanen, S., Palosaari, S., Kröger, H., Saarakkala, S.J., Herzog, W., Korhonen, R.K., Finnilä, M.A.J.J., 2021. Early changes in osteochondral tissues in a rabbit model of post-traumatic osteoarthritis. J. Orthop. Res. 39 (12), 2556–2567. https://doi.org/10.1002/jor.25009.

Intema, F., Sniekers, Y.H., Weinans, H., Vianen, M.E., Yocum, S.A., Zuurmond, A.M.M., DeGroot, J., Lafeber, F.P., Mastbergen, S.C., 2010. Similarities and discrepancies in subchondral bone structure in two differently induced canine models of osteoarthritis. J. Bone Miner. Res. 25, 1650–1657. https://doi.org/10.1002/jbmr.39.

Julkunen, P., Wilson, W., Isaksson, H., Jurvelin, J.S., Herzog, W., Korhonen, R.K., 2013. A review of the combination of experimental measurements and fibril-reinforced modeling for investigation of articular cartilage and chondrocyte response to loading. Comput. Math. Methods Med. 326150. https://doi.org/10.1155/2013/326150, 2013.

Kajabi, A.W., Casula, V., Ojanen, S., Finnilä, M.A., Herzog, W., Saarakkala, S., Korhonen, R.K., Nissi, M.J., Nieminen, M.T., 2020. Multiparametric MR imaging reveals early cartilage degeneration at 2 and 8 weeks after ACL transection in a rabbit model. J. Orthop. Res. 38, 1974. https://doi.org/10.1002/JOR.24644, 1986.

Kiviranta, I., Jurvelin, J., Säämänen, A.M., Helminen, H.J., 1985. Microspectrophotometric quantitation of glycosaminoglycans in articular cartilage sections stained with Safranin O. Histochemistry 82, 249–255. https://doi.org/10.1007/BF00501401.

Korhonen, R.K., Laasanen, M.S., Töyräs, J., Lappalainen, R., Helminen, H.J., Jurvelin, J.S., 2003. Fibril reinforced poroelastic model predicts specifically mechanical behavior of normal, proteoglycan depleted and collagen degraded articular cartilage. J. Biomech. 36, 1373–1379. https://doi.org/10.1016/S0021-9290(03)00069-1.

Lahm, A., Kreuz, P.C., Oberst, M., Maier, D., Haberstroh, J., Uhl, M., 2006. Subchondral and trabecular bone remodeling in canine experimental osteoarthritis. Arch. Orthop. Trauma Surg. 126, 582–587. https://doi.org/10.1007/s00402-005-0077-2.

Lane, L.B., Bullough, P.G., 1980. Age-related changes in the thickness of the calcified zone and the number of tidemarks in adult human articular cartilage. J. Bone Jt. Surg. Br. 62, 372–375.

Laverty, S., Girard, C.A., Williams, J.M., Hunziker, E.B., Pritzker, K.P.H., 2010. The OARSI histopathology initiative - recommendations for histological assessments of osteoarthritis in the rabbit. Osteoarthritis Cartilage 18, S53–S65. https://doi.org/10.1016/j.joca.2010.05.029.

Li, G., Moses, J.M., Papannagari, R., Pathare, N.P., DeFrate, L.E., Gill, T.J., 2006. Anterior cruciate ligament deficiency alters the in vivo motion of the tibiofemoral cartilage contact points in both the anteroposterior and mediolateral directions. J. Bone Jt. Surg. Am. 88, 1826–1834. https://doi.org/10.2106/JBJS.E.00539.

Li, G., Yin, J., Gao, J., Cheng, T.S., Pavlos, N.J., Zhang, C., Zheng, M.H., 2013. Subchondral bone in osteoarthritis: insight into risk factors and microstructural changes. Arthritis Res. Ther. 15, 223. https://doi.org/10.1186/ar4405.

Li, L.P., Soulhat, J., Buschmann, M.D., Shirazi-Adl, A., 1999. Nonlinear analysis of cartilage in unconfined ramp compression using a fibril reinforced poroelastic model. Clin. Biomech. 14, 673–682. https://doi.org/10.1016/S0268-0033(99)00013-3.

Liu, F., Kozanek, M., Hosseini, A., Velde, Van de, S.K., Gill, T.J., Rubash, H.E., Li, G., 2010. In-vivo tibiofemoral cartilage deformation during the stance phase of gait. J. Biomech. 43, 658–665. https://doi.org/10.1016/J.JBIOMECH.2009.10.028.

Malekipour, F., Hitchens, P., Whitton, R., Lee, P., 2020. Effects of in vivo fatigue-induced subchondral bone microdamage on the mechanical response of cartilage-bone under a single impact compression. J. Biomech. 100, 109594. https://doi.org/10.1016/J.JBIOMECH.2019.109594.

Malekipour, F., Oetomo, D., Lee, P.V.S., 2017. Subchondral bone microarchitecture and failure mechanism under compression: a finite element study. J. Biomech. 55, 85–91. https://doi.org/10.1016/j.jbiomech.2017.02.005.

Malekipour, F., Oetomo, D., Lee, P.V.S., 2016. Equine subchondral bone failure threshold under impact compression applied through articular cartilage. J. Biomech. 49, 2053–2059. https://doi.org/10.1016/j.jbiomech.2016.05.016.

Malekipour, F., Whitton, C., Oetomo, D., Lee, P.V.S., 2013. Shock absorbing ability of articular cartilage and subchondral bone under impact compression. J. Mech. Behav. Biomed. Mater. 26, 127–135. https://doi.org/10.1016/J.JMBBM.2013.05.005.

Manda, K., Wallace, R.J., Xie, S., Levrero-Florencio, F., Pankaj, P., 2017. Nonlinear viscoelastic characterization of bovine trabecular bone. Biomech. Model. Mechanobiol. 16, 173–189. https://doi.org/10.1007/s10237-016-0809-y.

Mehadji, B., Ahmed, Y., Berteau, J.P., 2019. A novel approach for computing 3D mice distal femur properties using high-resolution micro-computed tomography scanning. Micron 121, 1–7. https://doi.org/10.1016/J.MICRON.2019.02.011.

Mente, P.L., Lewis, J.L., 1994. Elastic modulus of calcified cartilage is an order of magnitude less than that of subchondral bone. J. Orthop. Res. 12, 637–647. https://doi.org/10.1002/jor.1100120506.

Mobasheri, A., Rayman, M.P., Gualillo, O., Sellam, J., Van Der Kraan, P., Fearon, U., 2017. The role of metabolism in the pathogenesis of osteoarthritis. Nat. Rev. Rheumatol. https://doi.org/10.1038/nrrheum.2017.50.

Mononen, M.E., Tanska, P., Isaksson, H., Korhonen, R.K., 2018. New algorithm for simulation of proteoglycan loss and collagen degeneration in the knee joint: data from the osteoarthritis initiative. J. Orthop. Res. 36, 1673–1683. https://doi.org/10.1002/JOR.23811.

Nagaraja, S., Couse, T.L., Guldberg, R.E., 2005. Trabecular bone microdamage and microstructural stresses under uniaxial compression. J. Biomech. 38, 707–716. https://doi.org/10.1016/j.jbiomech.2004.05.013.

Ojanen, X., Tanska, P., Malo, M.K.H., Isaksson, H., Väänänen, S.P., Koistinen, A.P., Grassi, L., Magnusson, S.P., Ribel-Madsen, S.M., Korhonen, R.K., Jurvelin, J.S., Töyräs, J., 2017. Tissue viscoelasticity is related to tissue composition but may not fully predict the apparent-level viscoelasticity in human trabecular bone – an experimental and finite element study. J. Biomech. 65, 96–105. https://doi.org/10.1016/j.jbiomech.2017.10.002.

Portier, H., Uk, S., Pallu, S., Jaffré, C., Chappard, C., 2020. Comparison of calcified cartilage between normal and osteoarthritis human knee specimens based on 3D synchrotron nano-computed tomography images with phase contrast: a preliminary study. Osteoarthritis Cartilage 28, S209–S210. https://doi.org/10.1016/J.JOCA.2020.02.341.

Pragnère, S., Boulocher, C., Pollet, O., Bosser, C., Levillain, A., Cruel, M., Hoc, T., 2018. Mechanical alterations of the bone-cartilage unit in a rabbit model of early osteoarthrosis. J. Mech. Behav. Biomed. Mater. 83, 1–8. https://doi.org/10.1016/j.jmbbm.2018.03.033.

Price, C., Li, W., Novotny, J.E., Wang, L., 2010. An in-situ fluorescence-based optical extensometry system for imaging mechanically loaded bone. J. Orthop. Res. 28, 805–811. https://doi.org/10.1002/JOR.21049.

Quasnichka, H.L., Anderson-Mackenzie, J.M., Bailey, A.J., 2006. Subchondral bone and ligament changes precede cartilage degradation in Guinea pig osteoarthritis. Biorheology 43, 389–397.

Radin, E.L., Rose, R.M., 1986. Role of subchondral bone in the initiation and progression of cartilage damage. Clin. Orthop. Relat. Res. 213, 34–40.

Räsänen, L.P., Tanska, P., Mononen, M.E., Lammentausta, E., Zbýň, Š., Venäläinen, M.S., Szomolanyi, P., van Donkelaar, C.C., Jurvelin, J.S., Trattnig, S., Nieminen, M.T., Korhonen, R.K., 2016. Spatial variation of fixed charge density in knee joint cartilage from sodium MRI – implication on knee joint mechanics under static loading. J. Biomech. 49, 3387–3396. https://doi.org/10.1016/j.jbiomech.2016.09.011.

Røhl, L., Linde, F., Odgaard, A., Hvid, I., 1997. Simultaneous measurement of stiffness and energy absorptive properties of articular cartilage and subchondral trabecular bone. Proc. Inst. Mech. Eng. Part H J. Eng. Med. 211, 257–264. https://doi.org/10.1243/0954411971534368.

Rytky, S.J.O., Huang, L., Tanska, P., Tiulpin, A., Panfilov, E., Herzog, W., Korhonen, R.K., Saarakkala, S., Finnilä, M.A.J., 2021. Automated analysis of rabbit knee calcified cartilage morphology using micro-computed tomography and deep learning. J. Anat. 239, 251–263. https://doi.org/10.1111/JOA.13435.

Sajjadinia, S.S., Haghpanahi, M., Razi, M., 2019. Computational simulation of the multiphasic degeneration of the bone-cartilage unit during osteoarthritis via indentation and unconfined compression tests. Proc. Inst. Mech. Eng. Part H J. Eng. Med. 233, 871–882. https://doi.org/10.1177/0954411919854011.

Sasazaki, Y., Shore, R., Seedhom, B.B., 2006. Deformation and failure of cartilage in the tensile mode. J. Anat. 208, 681–694. https://doi.org/10.1111/J.1469-7580.2006.00569.X.

Shaktivesh, Malekipour, F., Lee, P.V.S., 2019. Shock absorbing ability in healthy and damaged cartilage-bone under high-rate compression. J. Mech. Behav. Biomed. Mater. 90, 388–394. https://doi.org/10.1016/J.JMBBM.2018.10.023.

Sharma, A.R., Jagga, S., Lee, S.S., Nam, J.S., 2013. Interplay between cartilage and subchondral bone contributing to pathogenesis of osteoarthritis. Int. J. Mol. Sci. 14, 19805–19830. https://doi.org/10.3390/ijms141019805.

Shirazi, R., Shirazi-Adl, A., 2009. Computational biomechanics of articular cartilage of human knee joint: effect of osteochondral defects. J. Biomech. 42, 2458–2465. https://doi.org/10.1016/j.jbiomech.2009.07.022.

Sniekers, Y.H., Intema, F., Lafeber, F.P.J.G., Van Osch, G.J.V.M., Van Leeuwen, J.P.T.M., Weinans, H., Mastbergen, S.C., 2008. A role for subchondral bone changes in the process of osteoarthritis; a micro-CT study of two canine models. BMC Muscoskel. Disord. 9 https://doi.org/10.1186/1471-2474-9-20.

Spilker, R.L., Suh, J.K., Mow, V.C., 1992. A finite element analysis of the indentation stress-relaxation response of linear biphasic articular cartilage. J. Biomech. Eng. 114, 191–201. https://doi.org/10.1115/1.2891371.

Stender, M.E., Carpenter, R.D., Regueiro, R.A., Ferguson, V.L., 2016. An evolutionary model of osteoarthritis including articular cartilage damage, and bone remodeling in a computational study. J. Biomech. 49, 3502–3508. https://doi.org/10.1016/j.jbiomech.2016.09.024.

Stender, M.E., Regueiro, R.A., Ferguson, V.L., 2017. A poroelastic finite element model of the bone–cartilage unit to determine the effects of changes in permeability with osteoarthritis. Comput. Methods Biomech. Biomed. Eng. 20, 319–331. https://doi.org/10.1080/10255842.2016.1233326.

Stewart, H.L., Kawcak, C.E., 2018. The importance of subchondral bone in the pathophysiology of osteoarthritis. Front. Vet. Sci. 5, 178. https://doi.org/10.3389/fvets.2018.00178.

Tanska, P., Venäläinen, M.S., Erdemir, A., Korhonen, R.K., 2020. A multiscale framework for evaluating three-dimensional cell mechanics in fibril-reinforced poroelastic tissues with anatomical cell distribution – analysis of chondrocyte deformation behavior in mechanically loaded articular cartilage. J. Biomech. 101, 109648. https://doi.org/10.1016/j.jbiomech.2020.109648.

Turunen, S.M., Han, S.K., Herzog, W., Korhonen, R.K., 2013. Cell deformation behavior in mechanically loaded rabbit articular cartilage 4 weeks after anterior cruciate ligament transection. Osteoarthritis Cartilage 21, 505–513. https://doi.org/10.1016/j.joca.2012.12.001.

Venäläinen, M.S., Mononen, M.E., Jurvelin, J.S., Töyräs, J., Virén, T., Korhonen, R.K., 2014. Importance of material properties and porosity of bone on mechanical response of articular cartilage in human knee joint-A two-dimensional finite element study. J. Biomech. Eng. 136, 121005. https://doi.org/10.1115/1.4028801.

Venäläinen, Mononen, M.E., Salo, J., Räsänen, L.P., Jurvelin, J.S., Töyräs, J., Virén, T., Korhonen, R.K., 2016a. Quantitative evaluation of the mechanical risks caused by focal cartilage defects in the knee. Sci. Rep. 6, 37538. https://doi.org/10.1038/SREP37538.

Venäläinen, Mononen, M.E., Väänänen, S.P., Jurvelin, J.S., Töyräs, J., Virén, T., Korhonen, R.K., 2016b. Effect of bone inhomogeneity on tibiofemoral contact mechanics during physiological loading. J. Biomech. 49, 1111–1120. https://doi.org/10.1016/j.jbiomech.2016.02.033.

Verbruggen, S.W., Garrigle, M.J.M., Haugh, M.G., Voisin, M.C., McNamara, L.M., 2015. Altered mechanical environment of bone cells in an animal model of short- and long-term osteoporosis. Biophys. J. 108, 1587–1598. https://doi.org/10.1016/J.BPJ.2015.02.031.

Wang, S.X., Laverty, S., Dumitriu, M., Plaas, A., Grynpas, M.D., 2007. The effects of glucosamine hydrochloride on subchondral bone changes in an animal model of osteoarthritis. Arthritis Rheum. 56, 1537–1548. https://doi.org/10.1002/art.22574.

Wilson, W., Burken, van, C., Donkelaar, van, C., Buma, P., Rietbergen, van, B., Huiskes, R., 2006. Causes of mechanically induced collagen damage in articular cartilage. J. Orthop. Res. 24, 220–228. https://doi.org/10.1002/JOR.20027.

Wilson, W., Van Donkelaar, C.C., Van Rietbergen, B., Ito, K., Huiskes, R., 2004. Stresses in the local collagen network of articular cartilage: a poroviscoelastic fibril-reinforced finite element study. J. Biomech. 37, 357–366. https://doi.org/10.1016/S0021-9290(03)00267-7.

Xie, S., Manda, K., Wallace, R.J., Levrero-Florencio, F., Hamish, A., Simpson, R.W., Pankaj, P., 2017. Time dependent behaviour of trabecular bone at multiple load levels. Ann. Biomed. Eng. 45, 1219–1226. https://doi.org/10.1007/s10439-017-1800-1.

Zamli, Z., Robson Brown, K., Tarlton, J.F., Adams, M.A., Torlot, G.E., Cartwright, C., Cook, W.A., Vassilevskaja, K., Sharif, M., 2014. Subchondral bone plate thickening precedes chondrocyte apoptosis and cartilage degradation in spontaneous animal models of osteoarthritis. BioMed Res. Int. 606780. https://doi.org/10.1155/2014/606870, 2014.